Quantifying the Wind-Induced Bias of Rainfall Measurements for the Thies CLIMA Optical Disdrometer

E. Chinchella[1,2] ，A. Cauteruccio[1,2] ，and L. G. Lanza[1,2]

[1]Department of Civil, Chemical and Environmental Engineering, University of Genova, Genoa, Italy, [2]WMO Measurement Lead Centre "B. Castelli" on Precipitation Intensity, Genoa, Italy

Abstract The wind-induced bias of rainfall measurements obtained from non-catching instruments is addressed in this work with reference to the Laser Precipitation Monitor (LPM) optical disdrometer manufactured by Thies CLIMA. A numerical simulation approach is adopted to quantify the expected bias, involving three different models with increasing complexity. Computational Fluid-Dynamics simulation of the airflow field around the instrument with an embedded Lagrangian particle-tracking module to obtain raindrop trajectories are performed by solving the Unsteady Reynolds Averaged Navier-Stokes (URANS) equations and a Large Eddy Simulation (LES) model. URANS-uncoupled, LES-uncoupled, and LES-coupled approaches are tested to assess the impact of modeling the airflow turbulent fluctuations in detail. Due to the non-radially symmetric external shape of the instrument, various combinations of the wind speed and direction are considered. Catch ratios for monodisperse rain are obtained as a function of the particle Reynolds number and the wind direction and fitted to obtain site-independent curves to support application of the simulation results. Based on literature expressions to link the drop size distribution of real rainfall events with the rainfall intensity (which instead depend on the local rainfall climatology at the measurement site), sample collection efficiency curves are obtained from the catch ratios of monodisperse rain. The resulting adjustment curves allow rainfall measurements to be corrected using either a real-time or post-processing approach. However, at high wind speed and assuming that the wind blows parallel to the instrument sensing area, the instrument may fail to report precipitation altogether.

1. Introduction

Non-Catching Gauges (NCGs) are precipitation measurement instruments where liquid and solid precipitation is measured with no need of collecting the equivalent water volume in a reservoir. Each single hydrometeor is individually sensed, often using a contactless approach, providing a measure of the relevant microphysical properties of precipitation. The hydrometeor size and fall velocity are commonly measured by such instruments, also called disdrometers in this case.

The low maintenance requirements make NCGs quite suitable for use in automatic weather stations (AWSs) and play a significant role in their market share growth. NCGs are also the subject of increasing attention within the scientific community because of their potential contribution to several fields of research where the study of precipitation microphysical properties is addressed (see e.g. Adirosi et al., 2021; Johannsen et al., 2020).

NCGs, like the more traditional Catching-type Gauges (CGs), are not immune to both instrumental and environmental sources of measurement bias. The first category includes biases due to the instrument construction and measuring principle, while the latter one derives from the external conditions experienced by the instrument in the field. Amongst the environmental biases, wind is recognized as being responsible of considerable measurement biases for both CGs and NCGs (see e.g., Lanza & Cauteruccio, 2022).

Instrumental measurement biases are generally minimized through accurate instrument calibration. However, testing the performance of NCGs in the laboratory is not an easy task and—contrary to CGs whose calibration procedure is now standardised at least in Europe (CEN, 2019)—no agreed procedure exists for their traceable calibration (see Lanza et al., 2021). Recent developments on this subject were presented by Baire et al. (2022).

The wind-induced bias—first described by Jevons (1861) and known as the exposure problem or the Jevons effect—is due to the complex aerodynamic interactions arising between the airflow, the instrument body, and the approaching hydrometeors. The instrument, when immersed in a wind field, behaves like a bluff body obstacle,

producing strong velocity gradients and turbulence. Hydrometeors traveling near the instrument sensing area interact with the modified airflow field, deviating from their undisturbed trajectory and varying their fall speed.

For CGs, the exposure problem results in an undercatch bias since, on average, the number of hydrometeors that are swiped away by wind from the instrument collecting funnel exceeds the number of hydrometeors that are redirected inside it. The wind-induced undercatch was thoroughly investigated in the literature, and various correction curves were proposed based on different approaches: field intercomparisons (see e.g., Wolff et al., 2015), Wind Tunnel (WT) tests (see e.g. Green & Helliwell, 1972; Robinson & Rodda, 1969) and numerical simulation (see e.g. Cauteruccio et al., 2024; Colli et al., 2018; Nešpor & Sevruk, 1999). The consolidated approach largely employed in the literature to obtain a complete characterization of the measurement performance of precipitation gauges under windy conditions (both in shielded and unshielded configuration) requires the investigation of various combinations of wind speed, wind direction and hydrometeor characteristics (i.e., rain or snow, crystal type, particle shape and size). The available literature works generally assume that the instrument siting and installation is compliant with the recommendations of the World Meteorological Organization (WMO). Indeed, the quality of the measurement is very sensitive to the exposure of the instrument to the surrounding environment. Appropriate siting is therefore crucial to obtaining accurate precipitation measurements. The WMO Guide (WMO, 2018) specifies that the presence of obstacles and other instruments close to the precipitation gauge should be avoided, classifies the site of installation based on the distances for any obstacle and the land slope and suggests to deploy installations where wind is horizontal above the gauge orifice.

Efforts to quantify the wind-induced bias on rainfall measurements from NCGs are still scarce. One example is the work of Capozzi et al. (2021), where the wind-induced bias on a Laser Precipitation Monitor (LPM) manufactured by Thies CLIMA—Adolf Thies GmbH and Co. KG was evaluated in the field using measurements from a collocated tipping bucket rain gauge, proposing also a correction factor. The work of Capozzi et al. (2021) refers to a very specific, unorthodox installation of the Thies LPM, with the instrument installed on the top of a building above a vertical wall. The vertical velocity components generated by wind along this vertical surface cross the instrument body from the bottom. The instrument is also equipped with the wind shield provided by the manufacturer, which is ineffective against vertical wind and is characterized by an unusual bluff-body shape (Derakhshandeh & Alam, 2019) instead of the more aerodynamic shape that characterizes the Nipher shield (see Cauteruccio et al., 2024), the Single Alter wind shield (Alter, 1937) or the DFIR—Double Fence Intercomparison Reference (see Thériault et al., 2015). This means that the correction factor derived in Capozzi et al. (2021) is strictly site dependent and cannot be applied to measurements from the LPM when installed in a different configuration or in other measurement sites. Given the anticipated substantial impact of wind on the measurements, the deployment of comparable installations is strongly discouraged.

Further evidence of the impact of wind on measurements from specific NCGs is also shown in the work of Friedrich et al. (2013), where artifacts in the measured drop size distribution (DSD) were observed in data from a stationary OTT Parsivel laser disdrometer when compared against an identical gauge having automatic variable orientation and tilting mount used to continuously align it with the wind direction. Similar discrepancies were noted for the LPM in the work of Upton and Brawn (2008), where—even at limited wind speed—two such instruments installed with two different orientations (rotated by 90°) reported differences of up to 20% in the total number of detected hydrometeors.

Observed wind-induced biases were also reported for the two-Dimensional Video Disdrometer (2DVD) by Greenberg (2001), who noted a tendency to underestimate precipitation, with part of the sensing area of the instrument receiving no precipitation at all under some specific wind conditions. Further studies conducted by Testik and Pei (2017) on an improved version of the 2DVD showed that the effect of wind on precipitation is still present and that not only the measured precipitation amount and intensity are affected but also the DSD.

Quantification of the wind-induced bias for NCGs can be obtained using the same approaches used for CGs. However, the generally non-radially symmetric shape of such instruments implies a dependency of their aerodynamic behavior on the wind direction. This significantly increases the time and effort needed to evaluate the bias using field intercomparison and WT experiments. The numerical approach, instead, allows investigating many different configurations in terms of wind velocity and direction, gauge shape and precipitation type (see e.g., Cauteruccio, Chinchella, et al., 2021; Chinchella et al., 2024a), with acceptable cost and computational resources.

To the authors' knowledge, the first attempt to investigate the wind-induced bias for NCGs was presented by Nešpor et al. (2000). In that work, a two-dimensional video disdrometer (2DVD) was studied by means of numerical simulation concluding that the shape of the enclosure of the instrument causes errors in the detection of the small drops, some of them being counted more than once as they cross the sensing area while others are carried away. However, the outer shape of the instrument considered in that work is now obsolete and differs significantly from the current version. Furthermore, the 2DVD is a very special case of NCG, mostly used for research purposes in field test sites, while other NCGs—including the LPM—are more frequently used at operational measurement sites.

In the recent work of Chinchella et al. (2024a) the wind-induced bias was numerically quantified for the electroacoustic precipitation sensor Vaisala WXT520. Various combinations of the wind speed and direction were studied. Results show that the measured precipitation is overestimated by up to 400% under the influence of wind. Due to its measurement principle the shape of the Vaisala WXT520 gauge is very different from those of the LPM, therefore the derived adjustment curves are strictly instrument dependent.

For the specific case of the LPM, the complex airflow pattern around the instrument in windy conditions was initially investigated by Chinchella et al. (2021). In that work, a time independent numerical approach was used to compute velocity fields near the instrument body. The numerical results were thoroughly validated in the wind tunnel. The work highlighted the occurrence of significant airflow disturbances, but the trajectories of approaching hydrometeors and the resulting wind induced bias were not studied.

The present work is organized as follows. Section 2 presents a computationally expensive time-dependent numerical approach for computing the wind velocity field around the instrument body, and the embedded Lagrangian models used to compute hydrometeor trajectories are detailed. In Section 3, results from the time-dependent model are validated in the wind tunnel and compared against previous results. The simulated hydrometeor trajectories are presented and discussed for a range of rain drop diameters. Finally, in Section 4, the resulting wind induced bias is computed for monodisperse rain and for rain events, as a function of the rainfall intensity. Suitable best-fit relationships are provided for use in adjusting measured data, provided the necessary information about the wind speed and direction is available.

2. Methodology

This work focuses on the wind-induced bias of rainfall measurements obtained from the Laser Precipitation Monitor (LPM) (Thies, 2011), manufactured by Thies CLIMA—Adolf Thies GmbH and Co. KG. The instrument uses an optical transmission measuring principle and is widely adopted by researchers (see e.g., Adirosi et al., 2018; Bao et al., 2020; de Moraes Frasson et al., 2011; Iserloh et al., 2012). It is also used in operational measurement networks, thanks to its suitability for implementation in AWSs and relatively low cost (Pickering et al., 2019). The external shape is strongly non-radially symmetric, inducing a complex aerodynamic response when impacted by wind, as preliminarily shown in Chinchella et al. (2021).

The aerodynamic disturbance close to the instrument body is here modeled by means of a Computational Fluid Dynamic (CFD) simulation approach, employing different numerical schemes, to obtain the modified airflow velocity field in various configurations of the wind speed and direction. The simulation is performed using the open-source software library OpenFOAM (Jasak, 2009). Raindrop trajectories approaching the instrument are computed using the simulated airflow field as the input of an embedded Lagrangian Particle Tracking (LPT) model. Finally, the wind-induced bias is calculated for all simulated combinations of the raindrop size, wind speed and wind direction.

This numerical approach was first adopted by Nešpor and Sevruk (1999) on CGs with cylindrical shape, characterized by various design and thickness of the collector. The authors exploited CFD finite-volume simulations, solving the three-dimensional Reynolds Averaged Navier Stokes (RANS) equations by means of the k-ε turbulence closure model (where k is the turbulent kinetic energy and ε is the turbulent dissipation) over a quite coarse computational mesh.

A similar approach was used by Thériault et al. (2012) to simulate a shielded weighing gauge with chimney shape and by Colli et al. (2018), comparing different weighing and tipping-bucket gauges. In these latter cases, RANS simulations with a k-ω Shear Stress Transport (SST) closure model (Menter et al., 2003), with ω the specific rate of dissipation, were performed.
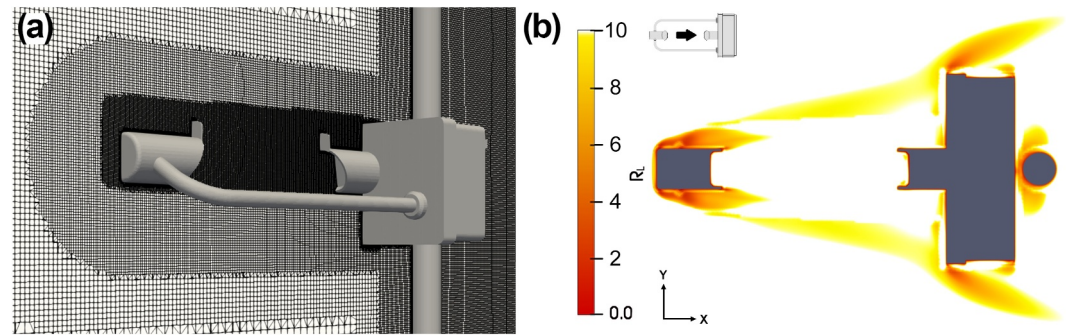
Figure 1. (a) Computational mesh along the longitudinal cross-section of the domain around the LPM at $Y = 0$ for the configuration at $\alpha = 0°$. (b) Map of the R_L ratio at $U_{ref} = 10$ m s^{-1} for $\alpha = 0°$, along the (X, Y) section at $Z = 0$. The black arrow indicates the undisturbed wind direction.

2.1. Numerical Airflow Simulation

The bluff-body behavior of the LPM when immersed in a wind field is quantified using both time-independent and time-dependent CFD simulations. First, the numerical solution of the Unsteady Reynolds Averaged Navier-Stokes (URANS) equations is borrowed from the work of Chinchella et al. (2021) to obtain the airflow field after a steady state condition is reached, under the hypothesis of stationary turbulence characteristics. Various combinations of the wind speed (from 2 to 20 m s^{-1}) and wind direction (from 0° to 180°) were simulated in that work, where the airflow field resulting from the time-independent approach is largely detailed and discussed, after suitable validation in the wind tunnel.

In the present work, we present a time-dependent approach based on the Large Eddy Simulation (LES) model (Piomelli, 1999) and compare results with the previously published time-independent approach. This allows us to numerically solve the scales of turbulence above a certain threshold, defined by a spatial filtering operation (usually bounded to the mesh size), while modeling only the smallest turbulent fluctuations using the Wall Adaptive Local Eddies (WALE) approach (Ducros et al., 1998).

A numerical model of the outer shape of the LPM (see Figure 1a and Chinchella et al., 2024b), including the supporting pole, is realised in the Standard Triangulation Language (STL) format. The longitudinal axis (X) is set along the main symmetry axis of the instrument, the vertical axis (Z) is directed upward, while the Y axis is normal to the (X, Z) plane. The origin of the reference system is in the center of the sensing area (the gauge laser infrared light beam). The simulation domain around the instrument is 4 m long in the X axis, 2.4 m wide along the Y axis, and 2 m high in the Z axis. The computational mesh has a maximum cell size of 0.04 m and is progressively refined down to 0.5 mm near the instrument walls to suitably model the turbulence generated by the gauge-flow interaction. Simulations were conducted by setting air as an incompressible fluid, with a density of 1.2 kg m^{-3} and a kinematic viscosity of 1.5×10^{-5} m^2 s^{-1}.

Two directions of the undisturbed wind are simulated, $\alpha = 0°$ (wind parallel to the laser beam) and $\alpha = 90°$ (wind perpendicular to the laser beam), maintaining the same definition of the angle α used in Chinchella et al. (2021). For each wind direction, two wind speed values (U_{ref}) equal to 5 and 10 m s^{-1} are tested. A sample (X, Z) section of the mesh at $Y = 0$ is presented in Figure 1a for the configuration at $\alpha = 0°$.

The suitability of the mesh refinements can be checked using the R_L criterion, where R_L is the ratio between the turbulence integral length scale and the grid length scale. This number is obtained after running precursor URANS simulations and represents the number of cells available to discretize the turbulent eddies (Pope, 2001). The computational mesh is progressively refined until the criterion $R_L \geq 10$ is satisfied in most of the domain. As reported in Figure 1b, showing the (X, Y) section of the domain at $Z = 0$, the R_L criterion is not met only in the proximity of the straight and sharp edges of the instrument body and in its immediate wake.

For the two wind directions investigated, $\alpha = 0°$ and $\alpha = 90°$, the final meshes contain about 19 and 25 million cells, respectively. The mesh size and quality parameters are listed in Table 1. Even considering the higher meshing requirements of the LES approach, these parameters fall in an acceptable range. A more in-depth explanation of the mesh quality parameters can be found in Aqilah et al. (2018) and Baker (2005).

Table 1
Mesh Size and Quality Parameters for the Two Wind Directions Investigated

Wind direction	No. of cells	Avg. non-orthogonality	Max non-orthogonality	Max skewness	Max aspect ratio
0°	19,729,994	4.70	49.95	3.32	15.58
90°	25,436,709	4.21	49.93	3.31	14.60

2.2. Lagrangian Particle Tracking

Drops with different size are affected by wind to a different extent, depending on their Stokes number (S_{tk}). Considerable deviation is expected for the trajectory of small-size drops ($S_{tk} \ll 1$), while large-size drops are almost undisturbed ($S_{tk} \gg 1$). Small-size drops are however the most abundant in natural rainfall events and account for a substantial portion of the total precipitation volume (for examples—assuming a DSD like the one proposed in the work of Cauteruccio and Lanza (2020)—drops with diameter up to 1 mm account for 93% of the total number of drops and 30% of the total water volume at a rainfall intensity of 10 mm h^{-1}. These percentages increase to 99% and 79%, respectively, if drops up to 2 mm in diameter are considered.

LPT models are generally divided in four main categories, according to their increasing complexity: uncoupled, one-, two- and four-way coupled models. The difference is in the amount of interaction that is considered between the fluid and the particles and between the particles themselves. The choice of the most suitable model is generally dictated by the volume fraction of particles in the domain, with higher values requiring more complex models.

Since the volume fraction of drops in the atmosphere during a rainfall event is generally low even at high rainfall rates (Uijlenhoet & Torres, 2006), the airflow is not influenced by the presence of water drops. Particle-to-particle interactions are also very limited, at least close to the ground where instruments are positioned. This means that uncoupled and one-way coupled models are sufficient to correctly model the interaction between the gauge, wind and precipitation. Furthermore, due to the typical time interval needed for a drop to cross the computational domain, varying between about 0.1 and 1 s, the assumption of a steady state condition for the wind field is also in reasonable accordance with typical field conditions.

Based on these considerations, two LPT models are tested in this work. Initially an uncoupled model is used, with the airflow field being initially computed while trajectories are obtained by solving the equation of motion (see e.g., Cauteruccio, Brambilla, et al., 2021) based on a stationary airflow velocity field (the steady state solution). To investigate the effect of turbulence on the drop trajectories, a second, one-way coupled model is also employed, which considers the evolution in time of the flow by advancing the CFD solution together with the computation of trajectories. This allows the effect of small-scale turbulent eddies on drops to be considered, although the computational burden is significantly increased. In both LPT models, particle-to-particle interactions are neglected. The uncoupled model is applied to CFD results obtained from both the URANS and the LES approach, using the time-averaged velocity fields as input. The one-way coupled model is used only in conjunction with the LES.

Water drops are injected in the computational domain along a variable spacing grid, 0.15 m wide and at least 0.45 m long. Grid length is increased—when necessary—for high wind speed and small hydrometeors diameter cases, to ensure that all possible trajectories that could potentially reach the gauge sensing area are simulated. All drops are tracked until they impact on the instrument body, the instrument sensing area or exit from the domain boundaries. The simulation stops once all released drops do impact on one of the domain boundaries or travel significantly below the instrument sensing area. Drops of diameter equal to 0.25, 0.5, 0.75 and from 1 mm up to 8 mm (with 1 mm increments) are simulated.

An in-depth analysis on the use of a LPT model for simulating drop trajectories and an extensive wind tunnel validation is presented by Cauteruccio, Brambilla, et al. (2021). The drag coefficient formulation used in that work is implemented here for various ranges of the particle Reynolds number, as established a priori among those proposed in the literature by Folland (1988) and formulated starting from data published by Beard (1976) and Khvorostyanov and Curry (2005).
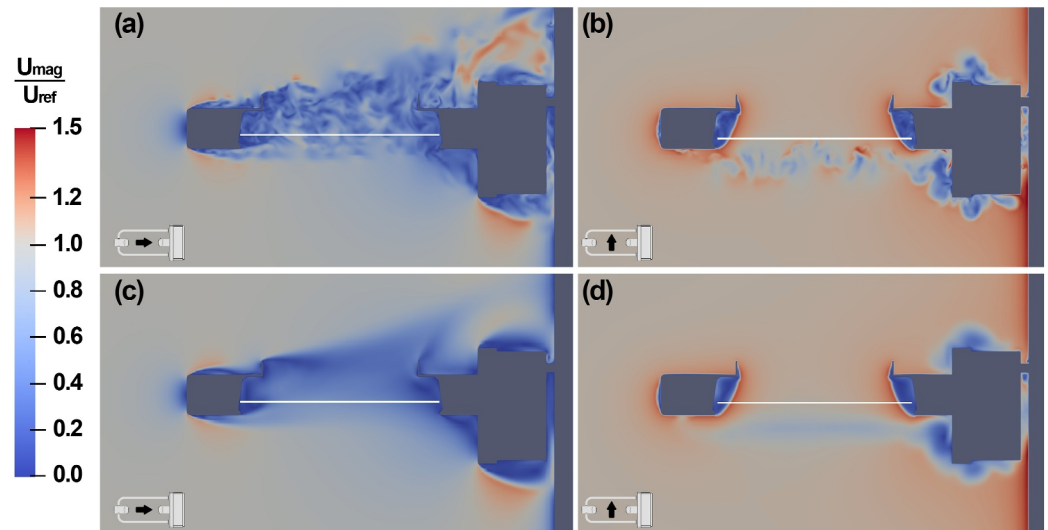
Figure 2. Instantaneous maps of the normalized velocity magnitude (U_{mag}/U_{ref}) from the LES at $U_{ref} = 10$ m s^{-1} for the wind directions (a) $\alpha = 0°$ and (b) $\alpha = 90°$. Time-averaged maps of the normalized velocity magnitude (U_{mag}/U_{ref}) from the LES at $U_{ref} = 10$ m s^{-1} for the wind directions (c) $\alpha = 0°$ and (d) $\alpha = 90°$. The visualized cross-sections are taken along the (X, Z) plane at $Y = 0$. The white horizontal line indicates the position of the sensing area (laser beam) of the instrument.

3. Numerical Simulations Results

3.1. Airflow Simulation

LES results are shown in Figure 2 in terms of maps of the normalized magnitude of the airflow velocity in the (X, Z) section of the domain at $Y = 0$, for $U_{ref} = 10$ m s^{-1} and $\alpha = 0°$ (panels (a) and (c)) and $90°$ (panels (b) and (d)), for both the instantaneous (panels (a) and (b)) and the average (panels (c) and (d)) configurations. The red zones indicate a larger magnitude of the flow velocity, U_{mag}, than the undisturbed wind speed, therefore $U_{mag}/U_{ref} > 1$, while in the blue zones the flow velocity is lower than the undisturbed wind speed, and $U_{mag}/U_{ref} < 1$.

At $\alpha = 0°$, the map of the instantaneous velocity magnitude (Figure 2a) shows strong recirculation and turbulence close to the instrument sensing area, due to the wind impacting on the instrument head. In terms of vertical velocity components (see Chinchella et al., 2024b), slight prevalence of the updraft is observed. The map of the averaged velocity magnitude (Figure 2c) shows an aerodynamic behavior that is close to the one shown in Chinchella et al. (2021), but with lower velocity gradients and a moderate influence of the updraft, like for the instantaneous flow field.

At $\alpha = 90°$, both the instantaneous (Figure 2b) and the average (Figure 2d) velocity fields show that the flow near the sensing area is mostly undisturbed. Especially in Figure 2b, the shedding of vortices generated by the supporting arms is clearly visible, having a limited influence on the velocity magnitude and remaining confined below the sensing area. Recirculation zones are concentrated near the receiving head, the instrument box, and the emitting head while turbulence close to the laser beam is minimal. In this case the aerodynamic behavior is identical to the time-independent simulation (Chinchella et al., 2021), only showing slightly lower velocity gradients, which may be due to turbulence induced diffusion that produces a smoothing effect.

Turbulence and vortex structures are highlighted, in Figure 3, near the instrument body by means of the Q-criterion (Hunt et al., 1988). At $\alpha = 0°$ (panel a), the wake generated by the instrument receiving head strongly affects the sensing area of the instrument and the flow region above it. At $\alpha = 90°$ (panel b), neither the turbulence structures produced by the two heads and the circuitry box, nor the turbulent wake produced by the supporting arm significantly affect the sensing area of the instrument.

The recirculation and vertical velocity components near the sensing area are stronger at $\alpha = 0°$, while the configuration at $\alpha = 90°$ presents limited flow disturbance. The effects of wind in the different instrument configurations are quantified here by considering a control volume 0.228 m long, 0.1 m high and 0.05 m wide, aligned with the instrument laser sheet and positioned just above it.
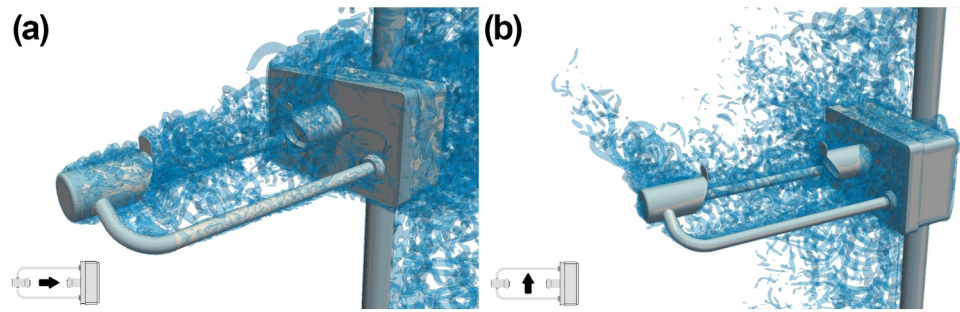
Figure 3. Visualization of the turbulent structures around the instrument using the Q-criterion at $U_{ref} = 10 \text{ m s}^{-1}$ for (a) $\alpha = 0°$ and (b) $\alpha = 90°$. The black arrows indicate the undisturbed wind direction.

Maximum and average values of the vertical velocity components inside the control volume are reported in Table 2. Results show larger maximum values of the updraft and downdraft (in both configurations) than those reported in Chinchella et al. (2021). The maximum updraft is doubled, the difference being equal to about 15% of U_{ref}, while the maximum downdraft is about three times larger, with a difference equal to about 30% of U_{ref}. Averages are also larger at $\alpha = 0°$, while differences are very limited at $\alpha = 90°$. For $\alpha = 0°$ the total volume where updraft is present is higher for the LES results with an increase of about 22% with respect to the same value shown in Chinchella et al. (2021).

The horizontal velocity components are also reported in Table 2. Average values of the longitudinal and transversal velocities from the LES simulations are in very good agreement with the URANS simulations of Chinchella et al. (2021), with differences below 1% of U_{ref}. However, their extreme values show larger differences, equal to about 5% of U_{ref} for longitudinal velocities and about 25% of U_{ref} for transversal velocities. Higher extreme values from LES results are however expected considering the smoothing effect due to the ensemble average performed by URANS simulations.

The longitudinal velocity is predominantly influenced by the flow blockage due to the instrument body. Maximum and average longitudinal velocities are therefore lower for $\alpha = 0°$ than for $\alpha = 90°$. The minimum longitudinal velocity reflects the presence of strong recirculation zones, quite widespread for $\alpha = 0°$, while they are limited and close to the instrument body for $\alpha = 90°$.

Transversal velocity components also show a clear difference between the two configurations, with larger extremes for the configuration at $\alpha = 90°$. The average velocity is always close to zero, indicating (as expected) that the flow is symmetrical for $\alpha = 0°$, while at $\alpha = 90°$, where the gauge surfaces are mostly parallel or perpendicular

Table 2
Normalized Updraft, Downdraft, Longitudinal and Transversal Velocity Components Within the Control Volume, Obtained From the LES for the Two Wind Speed Values Investigated

Wind direction	U_{ref} (m s^{-1})	Max updraft U_z/U_{ref}	Max downdraft U_z/U_{ref}	Avg. Updraft U_z/U_{ref}	Avg. Downdraft U_z/U_{ref}	% vol updraft	% vol downdraft
0°	5	0.399	0.475	0.115	0.081	96.321	3.679
0°	10	0.443	0.482	0.127	0.088	96.804	3.196
90°	5	0.404	0.474	0.023	0.045	72.908	27.092
90°	10	0.404	0.475	0.022	0.055	82.566	17.434

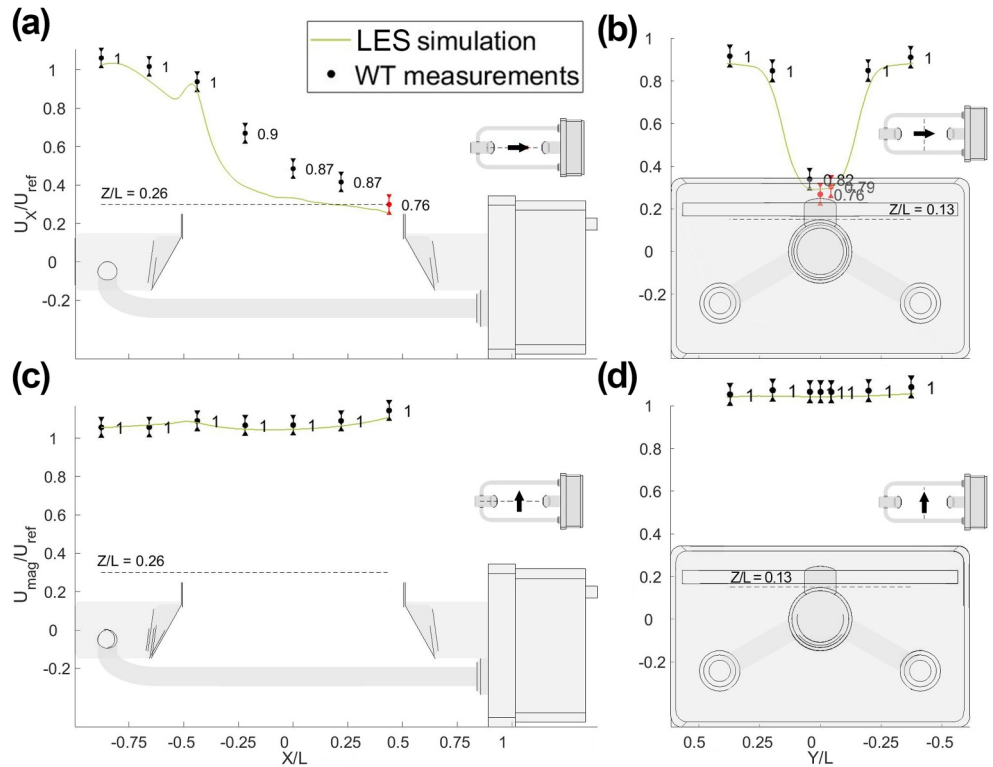| Wind Direction	U_{ref} (m s^{-1})	Max U_x/U_{ref}	Avg. U_x/U_{ref}	Min U_x/U_{ref}	Max U_y/U_{ref}	Avg. U_y/U_{ref}	Min U_y/U_{ref}
0°	5	0.957	0.334	−0.336	0.383	−0.001	−0.382
0°	10	0.950	0.341	−0.327	0.406	0.000	−0.402
90°	5	1.361	1.045	−0.345	0.969	0.022	−0.815
90°	10	1.359	1.052	−0.374	0.969	0.017	−0.810

Figure 4. Comparison of LES profiles (solid lines) of the magnitude of flow velocity against WT measurements (dots with one standard deviation bars) at $U_{ref} = 10 \ \mathrm{m \ s^{-1}}$. Two profiles (a),(c) parallel and (b),(d) perpendicular to the laser beam are shown for the configurations at (a),(b) $\alpha = 0°$ and (c),(d) $\alpha = 90°$. Numbers near each dot indicate the measurement quality as the ratio between the number of non-zero samples (over 30 s) and the total number of samples (over the same period).

to the flow, large maximum and minimum but low average values are obtained. Indeed, transversal velocity components are only present near the receiving and transmitting heads of the instrument.

3.2. Wind Tunnel Validation

An experimental campaign was conducted in the WT facility available at the Department of Civil, Chemical and Environmental Engineering (DICCA) of the University of Genova. Measurements were taken using a multi-hole pressure probe attached to a traversing arm with three degrees of freedom, and already used for validating the URANS model in Chinchella et al. (2021).

Measurements indicate that recirculation zones are well resolved, as shown in Figure 4 (panels (a) and (b)) where two profiles, one parallel and one transversal to the flow, are presented for $\alpha = 0°$.

However, as shown in Figure 4a, an even finer grid and possibly a wall resolving approach may be necessary to better resolve local turbulence generated by the extremely thin metal shields attached to the emitting and receiving heads. Their effect is averaged out by the ensemble average operated on turbulence by the URANS approach which is in good accordance with WT measurements since the probe itself operates a local average of the turbulent fluctuations, as shown in Chinchella et al. (2021).

On the contrary, considering the configuration at $\alpha = 90°$ (Figures 4c and 4d), the LES model results are in almost perfect accordance with both the WT measurements and the URANS simulation, meaning that (as expected) when recirculation is limited and the blockage produced by the instrument body is low, no tangible improvement is provided by the much more computationally expensive time dependent (LES) approach.

While, in general, there is good accordance between the two approaches, LES results show that turbulence modeling has a significant impact on the recirculation zone close to the instrument sensing area for the configuration at $\alpha = 0°$.
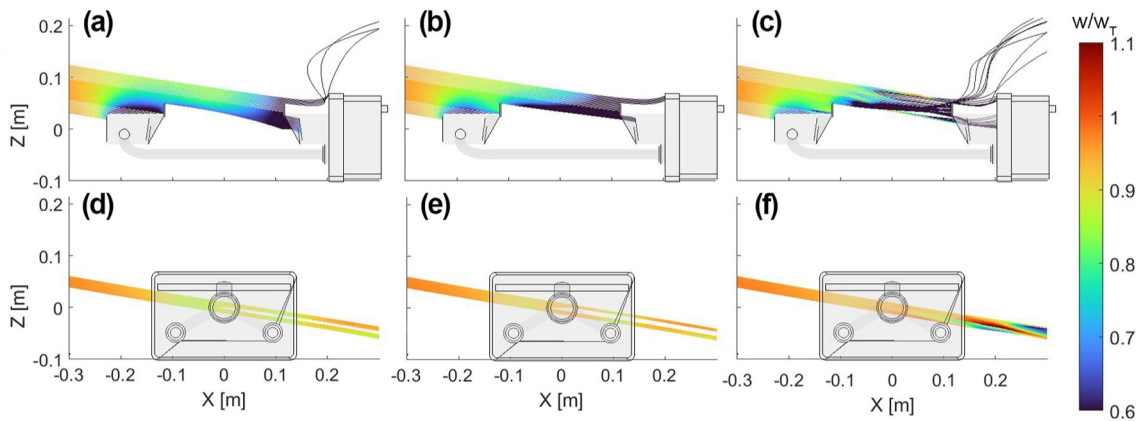
Figure 5. Simulated drop trajectories along the (X, Z) plane at $Y = 0$ and $U_{ref} = 5$ m s^{-1} for a drop diameter $D = 0.25$ mm. The (a),(d) URANS-uncoupled (b),(e) LES-uncoupled and (c),(f) LES-coupled results are presented for the configurations at (a,b,c) $\alpha = 0°$ and (d,e,f) $\alpha = 90°$. Trajectories are color coded according to the drop vertical velocity.

3.3. Hydrometeors Trajectories

Hydrometeor trajectories are calculated using the three combinations of the adopted CFD and LPT models, namely the URANS-uncoupled, LES-uncoupled, and LES-coupled approaches. A sample comparison of the results is shown in Figure 5 for drops with diameter $D = 0.25$ mm and $U_{ref} = 5$ m s^{-1}.

In all three cases, when wind blows parallel to the laser beam, a significant shielding effect of the gauge body is observed for small-size drops and medium to strong wind speed (see e.g., Figures 5a–5c). Light-weight drops, indeed, fall with a shallow slope and they are lost—due to the gauge body blockage—before even reaching its sensing area. Significant aerodynamic effects are also evident, producing a deviation of the trajectories and affecting the fall velocity. The two uncoupled models show very similar results, while for the coupled model additional variability occurs due to small scales eddies.

When the wind direction is perpendicular to the laser beam ($\alpha = 90°$) (Figures 5d–5f), the shielding and aerodynamic effects are very limited since the instrument offers the least amount of blockage to the flow in this configuration. A limited number of drops cross the laser beam outside of the expected sensing area, bypassing the sensor protective shield due to their very shallow angle of attack. This produces a limited amount of overcatch for some wind speed and drop size combinations. The two uncoupled models show no appreciable differences while the coupled model show noticeable velocity changes in trajectories past the gauge sensing area.

Large size drops (see Chinchella et al., 2024b) fall with a much steeper slope and are less influenced by the local airflow pattern ($S_{tk} >> 1$). The instrument shielding and aerodynamic effects have a reduced impact on trajectories and the fall velocities are practically unaffected. All three models produce therefore very similar results, meaning that small scale eddies do not significantly affect the behavior of large size drops.

4. The Wind-Induced Bias

4.1. Catch Ratios

Results of the LPT model are quantified in terms of the Catch Ratio (CR), defined per each drop diameter as the ratio between the number of drops that cross the instrument sensing area under the effect of wind and the number of drops that would have crossed the sensing area if the instrument was transparent to the wind and to the particle trajectories. The CRs are therefore a function of wind speed, wind direction and drop size and they are site independent. Results are presented here as a function of the particle Reynolds number (Re_p), computed as:

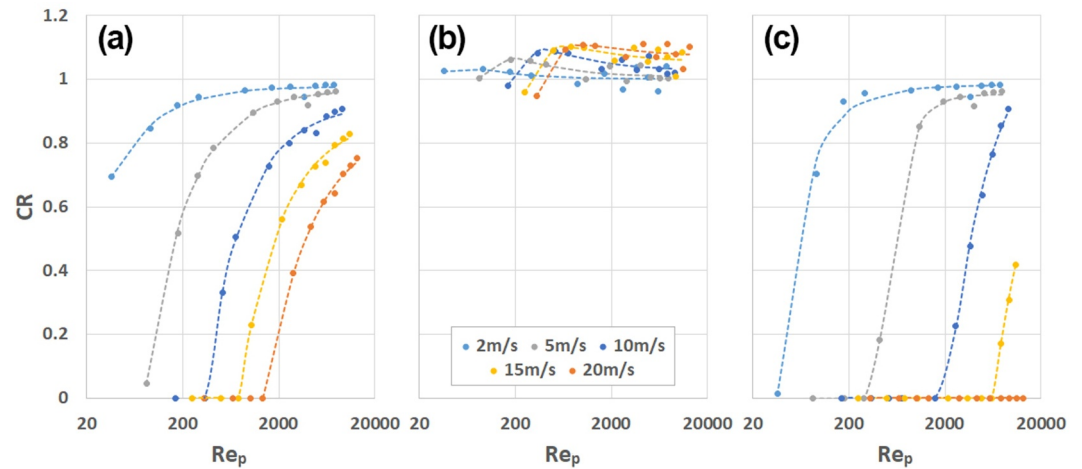$$Re_p = \frac{\sqrt{U_{ref}^2 + w_T^2} \cdot D}{\nu} \tag{1}$$

Figure 6. CR values as a function of Re_p obtained from the URANS-uncoupled model for the considered wind speed values in the configurations at (a) $\alpha = 0°$, (b) $\alpha = 90°$ and (c) $\alpha = 180°$. The dashed lines represent the best-fit function in the form of a second-order inverse polynomial.

where U_{ref} is the undisturbed wind speed, w_T is the hydrometeor terminal velocity, D is the drop diameter and ν is the kinematic viscosity of air (Pope, 2001).

For the URANS-uncoupled model, results are presented in Figure 6 for a few selected wind directions. Dots correspond to drop diameters of 0.25, 0.5, 0.75 and from 1 mm up to 8 mm (with 1 mm increments). When the wind is parallel to the laser beam (Figures 6a and c) significant biases are evident, and some drop size/wind speed combinations even occur with no one drop being sensed by the instrument. The bias—as expected—increases with the wind speed and decreases with Re_p, since larger drops are less affected by wind. Some non neglige-able bias is still present at high wind speed, even in the case of the largest drop size considered ($D = 8$ mm).

When the wind direction is perpendicular to the laser beam the bias is limited, with some minor overcatch that increases with the wind speed and the drop size (see Figure 6b). This is due to the sloped trajectory of large drops, which cross the gauge sensing area in unexpected positions otherwise precluded to vertically falling drops due to the shielding operated by the instrument.

At intermediate wind directions, the CR varies nonlinearly starting from a maximum at $\alpha = 90°$ and decreasing toward the two worst configurations at $\alpha = 0°$ and $\alpha = 180°$. By using the particle Reynolds number as the independent variable, the CR can be fitted—in the range of values investigated—by a second-order inverse polynomial function, as follows:

$$CR(Re_p, U_{ref}, \alpha) = a(U_{ref}, \alpha) + \frac{b(U_{ref}, \alpha)}{Re_p} + \frac{c(U_{ref}, \alpha)}{Re_p^2} \qquad (2)$$

where the three parameters a, b, and c are a function of the wind speed (U_{ref}) and direction (α). Best-fit values of the parameters are reported in Tables A1–A3 while their coefficient of determination is shown in Table A4 (see Appendix A) for the examined combinations of wind speed and direction.

The best-fit curves of the CR values calculated from the URANS-uncoupled results (dashed lines) are compared in Figure 7 against the LES-uncoupled model results (dots) and the LES-coupled model results (triangles). When wind blows parallel to the laser beam, the two uncoupled approaches provide almost identical results. When the wind direction is perpendicular to the laser beam, results are still in good accordance, but some dispersion occurs in the CR values. Larger differences are present for small size drops ($D = 0.25$ mm), with considerably lower CR values if compared with the URANS-uncoupled results.

This suggests that the considerable computational burden of the LES-uncoupled approach does not provide significant improvement over the much cheaper URANS-uncoupled approach. The impact of the small
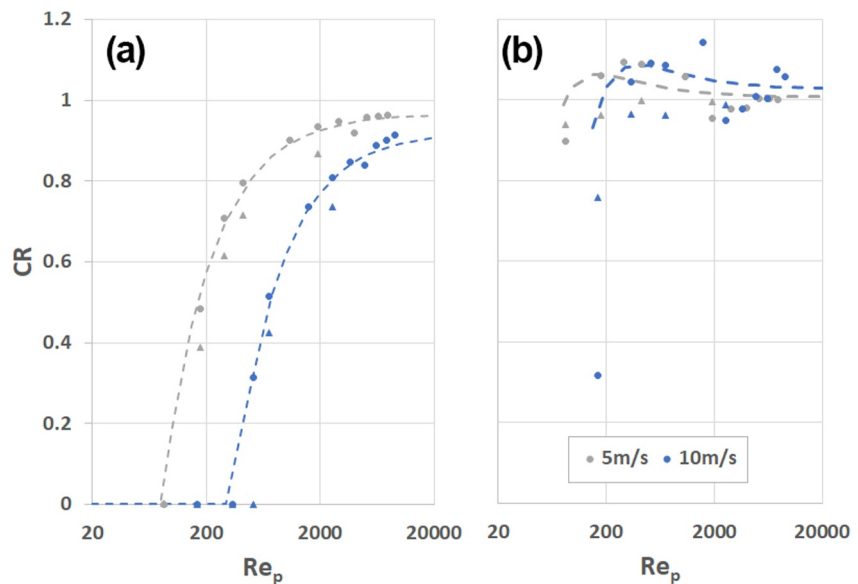
Figure 7. CR values obtained from the LES-uncoupled model (dots) and LES-coupled model (triangles) as a function of Re_p for the configurations at (a) $\alpha = 0°$ and (b) $\alpha = 90°$ and for the two considered wind speed values. The dashed lines represent the best-fit functions obtained for the URANS-uncoupled approach, used as a reference.

differences in the velocity field on raindrop trajectories, already noted at $\alpha = 0°$, is therefore negligeable, the primary factor controlling the results being the instrument shape.

The comparison between the best-fit curves of the URANS-uncoupled results (dashed lines) and the LES-coupled model results (triangles) shows CRs characterized by the same behavior but with overall lower values for both the considered wind directions. The explanation can be found in the enhanced trajectory deviations produced by turbulence, which may divert some hydrometeors away from the laser beam. This suggests that small scale eddies close to the instrument body introduce non negligeable effects, even for medium size drops.

The deviation of drop trajectories, however, depends on the instantaneous velocity fluctuations in the recirculation zone, which are intrinsically turbulent. Therefore, the opposite effect might also be observed for drops released in the wind field at a different instant in time. To assess the influence of small-scale eddies, a statistically relevant number of simulations should be run (for each combination of the considered drop size and wind speed and direction), by varying the injection time of the drops in the domain. This is hardly feasible in practice due to the high computational burden of this approach.

4.2. The Collection Efficiency

While the CRs are the primary results of the numerical simulation approach, before the wind-induced bias on the measurement of precipitation integral properties (e.g., RI) can be quantified, a specific precipitation climatology (and therefore a specific DSD as a function of precipitation intensity) must be assumed. The DSD can be either directly measured by the instrument (after calibration and correction of the wind-induced bias) on site or derived from literature data. Quantification of the wind-induced bias is here performed by considering the CRs obtained from the URANS-uncoupled approach and assuming the DSD proposed in the work of Cauteruccio and Lanza (2020) as an example. This is an exponential DSD (Marshall & Palmer, 1948), with the intercept N_0 (mm^{-1} m^{-3}) and slope Λ (mm^{-1}) being a power law function of RI (mm h^{-1}) in the form:

$$N_0 = 835.91 \cdot RI^{0.8942} \tag{3}$$

$$\Lambda = 3.2863 \cdot RI^{-0.076} \tag{4}$$

The wind-induced bias on RI measurements is computed in terms of the Collection Efficiency (CE), defined as the ratio between the total amount of precipitation that effectively crosses the sensing area of the instrument and the
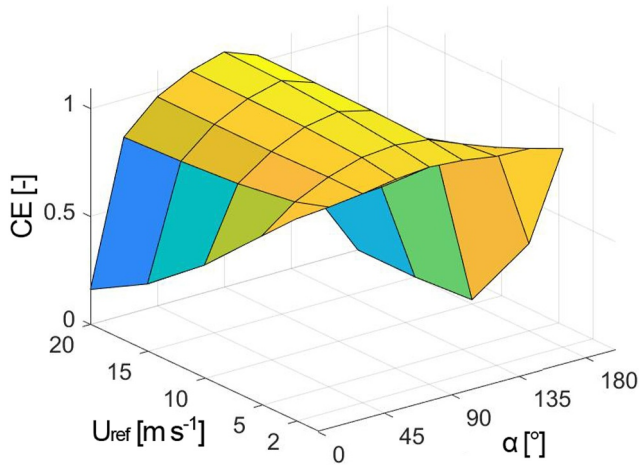
Figure 8. Collection efficiency surface for the LPM as a function of the undisturbed wind speed (U_{ref}) and wind direction (α) computed considering the DSD from Cauteruccio and Lanza (2020) and RI = 10 mm h^{-1}.

ideal amount that would have crossed it in the absence of any disturbance (therefore normalized with the collected volume for unit CR). Once the number of drops of each diameter D in a cubic meter of air per unit size bin N (D,RI) is known (from the chosen DSD), the numerical collection efficiency is obtained as:

$$CE(U_{ref}, \alpha, RI) = \frac{\int_0^{d_{max}} V(D) \cdot CR(D, U_{ref}, \alpha) \cdot N(D,RI) \cdot dD}{\int_0^{d_{max}} V(D) \cdot N(D,RI) \cdot dD} \qquad (5)$$

where $V(D)$ is the volume of the drop of diameter D. The CE is therefore a function of the wind velocity (U_{ref}), wind direction (α) and rainfall intensity (RI), with Equation 5 representing a 3-D surface rather than the typical 2-D curve obtained for axial-symmetric instruments.

The CE of the LPM, obtained from Equation 5, is represented in the graph of Figure 8 using the CRs obtained from numerical simulation and assuming a precipitation intensity RI = 10 mm h^{-1}. The CE surface shows that wind direction is the primary influencing factor for the instrument performance according to its specific geometry. For the configuration at $\alpha = 0°$ or close to $\alpha = 180°$ the collection efficiency drops considerably, even at moderate and low wind speed. Meanwhile, at about $\alpha = 90°$, the instrument performance is close to ideal, showing just a slight overcatch at high wind speed.

The CE tends to increase with the RI—as shown in Figure 9—because the wind-induced bias tends to decrease with increasing RI. This is expected since the number of large drops that are progressively less affected by wind increases in any precipitation event with increasing RI. At $\alpha = 90°$, the CE slightly decreases with RI at any wind speed since also in the case of overcatch, very large drops are less influenced by wind than medium and smaller ones.

In the RI range between 0.5 mm h^{-1} and 500 mm h^{-1}, the CE for all combinations of wind speed and direction are well fitted by a power law in the form:

$$CE = m \cdot RI^n \qquad (6)$$

where m (U_{ref}, α) and n (U_{ref}, α) are the two fitting parameters, whose values are reported in Tables A5 and A6 while their respective coefficient of determination is shown in Table A7 (see Appendix A).
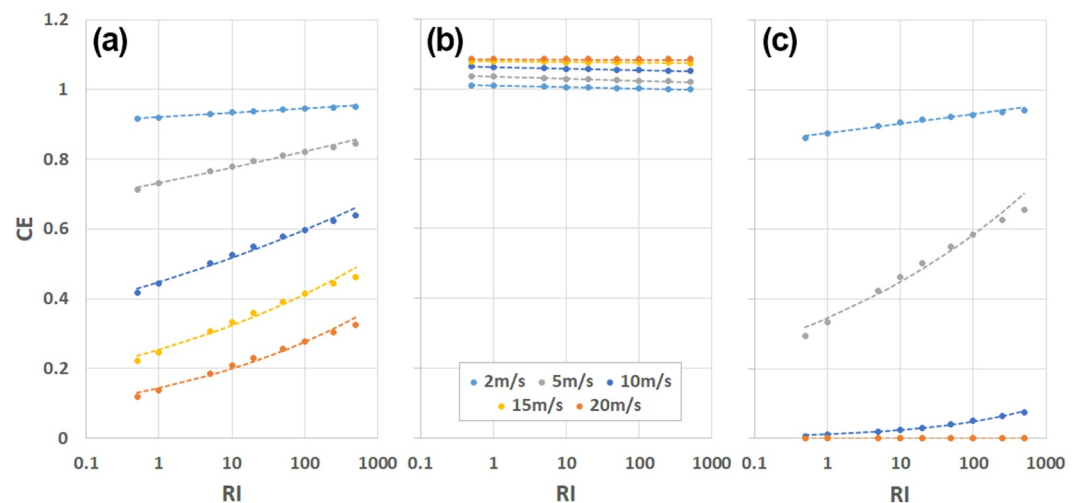

Figure 9. The collection efficiency of the LPM as a function of wind speed (U_{ref}) and rainfall intensity (RI) for the considered combinations of wind speed and direction, at (a) $\alpha = 0°$, (b) $\alpha = 90°$ and (c) $\alpha = 180°$ based on the URANS-uncoupled model. Dashed lines represent the best-fit functions in the form of power laws.
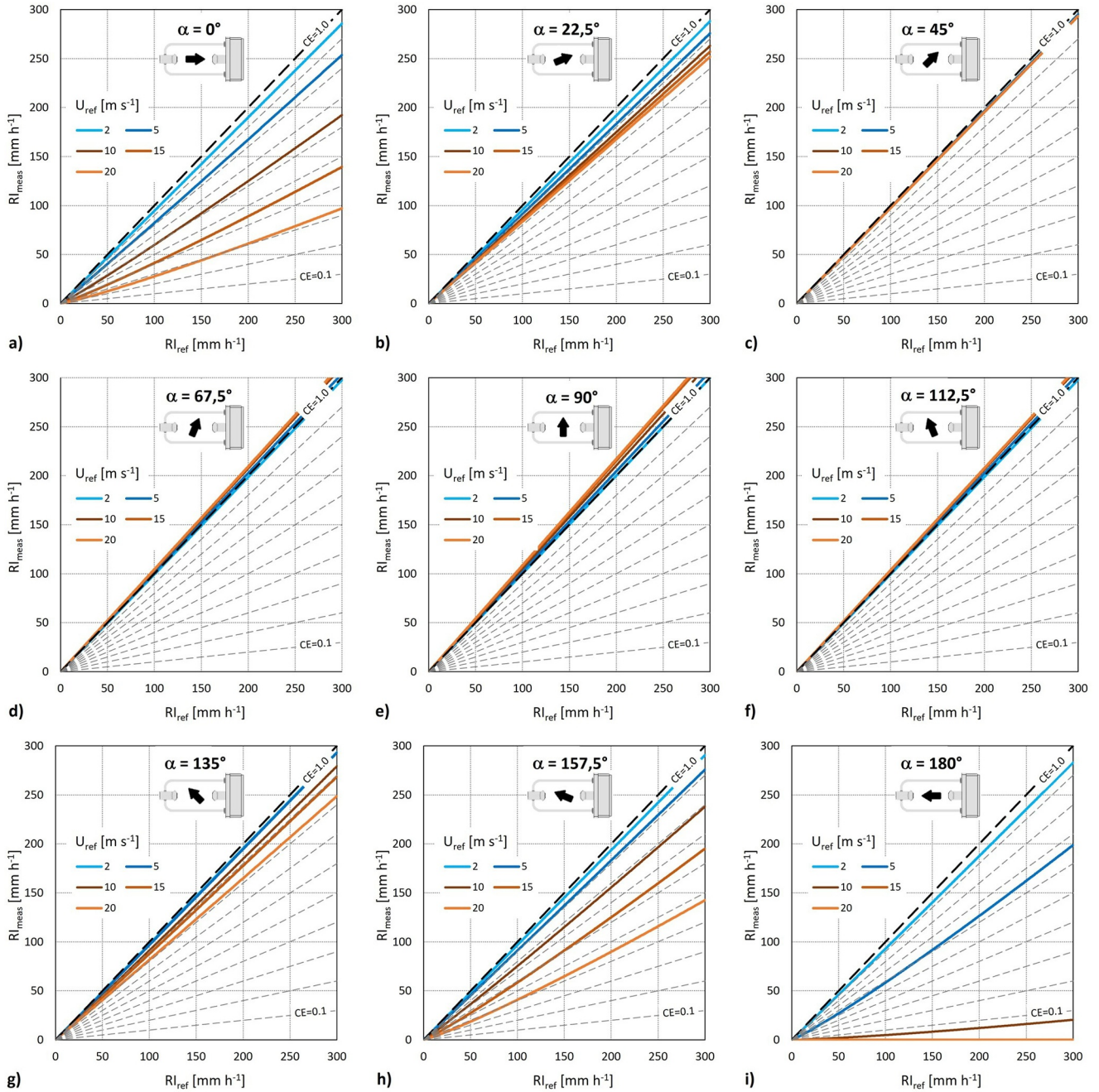
Figure 10. Correction curves (solid lines) for the LPM as a function of wind speed (line color) and direction (angle α with reported schematics) for a rainfall intensity range between 0- and 300- mm h^{-1}. Dashed lines represent the constant CE curves for CE values between 0 and 1, at 0.1 intervals.

From Equation 6 and considering the definition of the CE (Equation 5), the actual rainfall intensity, RI_{ref}, can be obtained from the rainfall intensity measured by the instrument, RI_{meas}, using the following expression:

$$RI_{ref} = \left(\frac{RI_{meas}}{m}\right)^{\frac{1}{n+1}} \tag{7}$$

This result is suitable for either real time or a posteriori adjustment of the measured data, providing that the environmental conditions (wind speed and direction) are known. It fails, however, for high wind speed and $\alpha = 180°$ since the instrument may fail to report precipitation altogether in such conditions. Positioning the

instrument at $\alpha = 180°$, based on the prevailing wind climatology at the measurement site, should be therefore avoided in the field.

The obtained correction curves for the nine investigated wind directions are summarized in Figure 10 within a range of 0–300 mm h^{-1} and compared with the straight lines corresponding to a constant CE, for CE values between 0 and 1 (displayed at 0.1 intervals).

5. Conclusions

The wind-induced bias of rainfall intensity measurements made by using the LPM was quantified using three numerical simulation models with increasing complexity. The comparison of the results obtained with two CFD-LPT uncoupled models showed that the small differences obtained in the simulated airflow field produce negligeable effects on the CRs. Instead, the instrument shape—and the blockage thereof—was found to be the primary factor in controlling the magnitude of the wind-induced bias, due to the non-radially symmetric shape of the LPM. The worst performing condition occurs when wind blows parallel to the laser beam, since the instrument offers the maximum blockage to the airflow due to the presence of the electronic box, while the best performing orientation is when the wind direction is perpendicular to the laser beam, since blockage is minimal.

The LES-coupled model highlights the effect of small-scale eddies, which induce non negligeable deviations of the drop trajectories and result in significantly lower CRs. Since they are a product of turbulence—and therefore fluctuating in nature—a statistically relevant number of simulations performed by varying the drop release time are needed to quantify their influence on the CRs. The computational cost of such analysis would be at least one order of magnitude larger than the one borne for the present work. To allow considering a wide range of environmental conditions (both in terms of wind speed and direction) and due to the limited differences shown between the three numerical approaches tested (other than the high computational cost of LES based simulations), correction curves were derived starting from the URANS-uncoupled simulation.

The behavior of the instrument under the effect of wind is site-independent, and the impact on specific mono-disperse rain measurements only depends on the wind speed and direction. A specific local climatology must be assumed before correction for the wind-induced bias on real RI measurements can be derived. The procedure was exemplified here for a literature DSD and can be easily applied to any given DSD, including the measured one, tailoring results to any specific installation site—provided the wind speed and direction are known.

Our results show that the significant measurement bias of the LPM can exceed the bias often observed for more traditional CGs under the effect of wind. The bias cannot be overlooked and raises the question of the reliability of the measurements obtained from this instrument in the field in windy conditions. The measured rainfall data should be therefore treated with caution and properly adjusted before use. Adjustments may account for a significant percentage of the rainfall totals in sites where wind is common during low to moderate rainfall intensity events. The resulting bias on the measured DSD under windy conditions is expected to be significant as well. This aspect is still under development and would require including the impact of instrumental (calibration) biases.

Considerable modifications of the instruments design would be required to minimize the magnitude of the wind-induced bias. Adjustment of the measured data according to the correction function proposed in this work is instead a suitable alternative. In any case, the instrument should be positioned in the field with an orientation that favors the occurrence of wind from a direction perpendicular to the laser beam. However, optical issues require instead that the instrument is aligned with the receiving head toward south (in the northern hemisphere), to minimize chances of direct sunlight reaching the sensor. This suggests that for unfavorable sites shielding against wind may be a necessity for such instruments.

The results obtained also indicate that similar measurement biases can occur with other NCGs that use the same measuring principle and do not have a radially symmetrical shape.

Application and testing of the proposed correction curves to real-world disdrometer measurements is not straightforward and suffer from the shortage of suitable data sets. A few existing, publicly accessible disdrometer archives are available such as the DiVeN network (Pickering et al., 2019), the Italian Disdrometer Network (Adirosi et al., 2023) and the DISDRODB database (Ghiggi et al., 2023). However, even when anemometers are installed at the measurement sites, archives often do not provide the necessary information about wind speed and direction, or the anemometer is installed at a significantly higher elevation than the disdrometer. In many cases,

the reference instrument is not present and disdrometers are installed in configurations that are not compliant with the specifications of the WMO (e.g., on top of building roofs, on sloped ground, at non-standard height, etc.) and the derived impact of wind on the measurements would therefore result in a very site-specific information.

Limitations of the presented approach include having neglected the potential role of the free-stream turbulence in the simulation, that is, the inherent level of turbulence that is present in the real-world wind field. It is assumed that the impact of free-stream turbulence is minor with respect to that of turbulence generated by the interaction of the wind field with the instrument body. However, some dependency on the precipitation intensity (and the associated DSD) can be expected. Moreover, raindrops are assumed to be spherical, and the formulation used for the drag coefficient used in the simulation is derived based on this assumption. In natural precipitation, only drops with diameter below 1 mm can be considered approximately spherical. Larger drops are flattened by the dynamic pressure exerted by the surrounding air, and their axial ratio between the vertical and the horizontal axis deviates from unity (see e.g. Lanza et al., 2021). The resulting drag coefficient would be slightly different from the one assumed in this work and depending on the trajectory of the drop relative to the wind velocity.

The validation of the proposed correction curves with real-world disdrometer data would further require the availability of reference instruments at the measurement site (specifically instruments that are either not or minimally affected by the wind induced bias), like the experimental sites set up for the WMO intercomparison of rainfall intensity gauges (both CGs and NCGs) organized from 2007 to 2009 in Vigna di Valle, Italy (Lanza & Vuerich, 2009) and the large number of experimental sites employed in different countries during the WMO Solid Precipitation Intercomparison Experiment (SPICE) from 2012 to 2015 (Kochendorfer et al., 2022).

Appendix A

In this appendix, the values of the parameters used to derive the best-fit curves of CR and CE are listed.

Table A1
Numerical Values of the Parameter a (U_{ref}, α)

	$\alpha = 0°$	$\alpha = 22.5°$	$\alpha = 45°$	$\alpha = 67.5°$	$\alpha = 90°$	$\alpha = 112.5°$	$\alpha = 135°$	$\alpha = 157.5°$	$\alpha = 180°$
$U_{ref} = 2$ m s^{-1}	0.978	0.985	0.985	0.992	1.001	0.992	0.985	0.986	0.983
$U_{ref} = 5$ m s^{-1}	0.967	0.966	0.985	0.994	1.007	0.998	0.991	0.968	0.950
$U_{ref} = 10$ m s^{-1}	0.923	0.936	1.000	1.021	1.027	1.025	1.024	0.928	1.186
$U_{ref} = 15$ m s^{-1}	0.880	0.914	0.994	1.038	1.056	1.042	1.022	0.908	1.001
$U_{ref} = 20$ m s^{-1}	0.849	0.901	0.986	1.045	1.072	1.046	1.000	0.911	0.000

Table A2
Numerical Values of the Parameter b (U_{ref}, α)

b	$\alpha = 0°$	$\alpha = 22.5°$	$\alpha = 45°$	$\alpha = 67.5°$	$\alpha = 90°$	$\alpha = 112.5°$	$\alpha = 135°$	$\alpha = 157.5°$	$\alpha = 180°$
$U_{ref} = 2$ m s^{-1}	−12.115	−10.441	−3.127	1.671	3.987	2.715	0.104	−7.928	−13.202
$U_{ref} = 5$ m s^{-1}	−79.572	−30.881	−7.169	13.938	19.497	10.87	−12.488	−26.282	29.366
$U_{ref} = 10$ m s^{-1}	−299.117	−68.865	−23.311	20.891	47.524	14.389	−134.307	8.653	−2679.583
$U_{ref} = 15$ m s^{-1}	−716.663	−99.301	−24.044	22.634	60.640	14.869	−215.436	57.951	−6383.994
$U_{ref} = 20$ m s^{-1}	−1434.513	−128.315	−12.406	28.641	69.399	21.130	−274.166	151.993	0.000

Table A3
Numerical Values of the Parameter c (U_{ref}, α)

c	$\alpha = 0°$	$\alpha = 22.5°$	$\alpha = 45°$	$\alpha = 67.5°$	$\alpha = 90°$	$\alpha = 112.5°$	$\alpha = 135°$	$\alpha = 157.5°$	$\alpha = 180°$
$U_{ref} = 2$ m s^{-1}	62.757	185.971	13.358	−89.596	−113.154	−190.780	−258.741	238.735	−816.477
$U_{ref} = 5$ m s^{-1}	132.720	1127.165	−99.925	−1590.934	−1674.908	−1913.006	−2497.880	−880.128	−148793.884
$U_{ref} = 10$ m s^{-1}	−4768.011	6656.178	642.237	−6601.725	−9275.088	−8551.494	6965.837	−111300.964	415,171.710
$U_{ref} = 15$ m s^{-1}	36,236.461	16,558.008	−1355.511	−14845.244	−21270.653	−20790.352	18,699.213	−618261.523	582.429
$U_{ref} = 20$ m s^{-1}	384,125.964	31,059.792	−8744.195	−27936.357	−37064.360	−40791.453	29,387.632	−3005808.649	0.000

Table A4
Coefficient of Determination for the Best Fit of the CR

R^2	$\alpha = 0°$	$\alpha = 22.5°$	$\alpha = 45°$	$\alpha = 67.5°$	$\alpha = 90°$	$\alpha = 112.5°$	$\alpha = 135°$	$\alpha = 157.5°$	$\alpha = 180°$
$U_{ref} = 2$ m s^{-1}	0.9835	0.9969	0.5610	0.9432	0.1617	0.9944	0.9059	0.9780	0.9924
$U_{ref} = 5$ m s^{-1}	0.9986	0.9972	0.8460	0.9328	0.6111	0.9571	0.9733	0.9992	0.9994
$U_{ref} = 10$ m s^{-1}	0.9987	0.9920	0.8838	0.9624	0.7768	0.9863	0.9785	0.9995	0.9992
$U_{ref} = 15$ m s^{-1}	0.9990	0.9924	0.8550	0.9977	0.7148	0.9992	0.9767	0.9998	0.9999
$U_{ref} = 20$ m s^{-1}	0.9992	0.9695	0.8903	0.9998	0.7982	0.9999	0.9597	0.9996	–

Table A5
Numerical Values of the Fitting Parameter m (U_{ref}, α) as a Function of Wind Speed and Direction

m	$\alpha = 0°$	$\alpha = 22.5°$	$\alpha = 45°$	$\alpha = 67.5°$	$\alpha = 90°$	$\alpha = 112.5°$	$\alpha = 135°$	$\alpha = 157.5°$	$\alpha = 180°$
$U_{ref} = 2$ m s^{-1}	0.9208	0.9408	0.9666	0.9938	1.0097	0.9935	0.9655	0.9583	0.8754
$U_{ref} = 5$ m s^{-1}	0.7326	0.8879	0.9655	1.0159	1.0353	1.0075	0.9268	0.8742	0.3443
$U_{ref} = 10$ m s^{-1}	0.4482	0.8479	0.9602	1.0303	1.0631	1.0155	0.8362	0.6006	0.0121
$U_{ref} = 15$ m s^{-1}	0.2539	0.8301	0.9622	1.0357	1.0794	1.0184	0.8043	0.3736	0.0000
$U_{ref} = 20$ m s^{-1}	0.1447	0.8191	0.9648	1.0388	1.0866	1.0196	0.7680	0.2173	0.0000

Table A6
Numerical Values of the CE Fitting Parameter n (U_{ref}, α) as a Function of Wind Speed and Direction

n	$\alpha = 0°$	$\alpha = 22.5°$	$\alpha = 45°$	$\alpha = 67.5°$	$\alpha = 90°$	$\alpha = 112.5°$	$\alpha = 135°$	$\alpha = 157.5°$	$\alpha = 180°$
$U_{ref} = 2$ m s^{-1}	0.0059	0.0037	0.0021	−0.0002	−0.0018	0.0000	0.0023	0.0019	0.0131
$U_{ref} = 5$ m s^{-1}	0.0252	0.0061	0.0033	−0.0004	−0.0023	0.0010	0.0092	0.0088	0.1148
$U_{ref} = 10$ m s^{-1}	0.0628	0.0059	0.0032	0.0012	−0.0019	0.0030	0.0188	0.0488	0.3032
$U_{ref} = 15$ m s^{-1}	0.1060	0.0055	0.0029	0.0013	−0.0007	0.0033	0.0187	0.0972	0.8463
$U_{ref} = 20$ m s^{-1}	0.1412	0.0043	0.0025	0.0016	−0.0001	0.0036	0.0134	0.1371	0.0000

Table A7
Coefficient of Determination for the Best Fit of the CE

R^2	$\alpha = 0°$	$\alpha = 22.5°$	$\alpha = 45°$	$\alpha = 67.5°$	$\alpha = 90°$	$\alpha = 112.5°$	$\alpha = 135°$	$\alpha = 157.5°$	$\alpha = 180°$
$U_{ref} = 2$ m s^{-1}	0.9878	0.9852	0.9806	0.9756	0.9735	0.9912	0.9949	0.9952	0.9979
$U_{ref} = 5$ m s^{-1}	0.9997	0.9982	0.9916	0.9989	0.9974	0.9947	0.9965	0.8788	0.9523
$U_{ref} = 10$ m s^{-1}	0.9602	0.9639	0.9787	0.9857	0.9943	0.9837	0.8838	0.0475	0.8435
$U_{ref} = 15$ m s^{-1}	0.9743	0.9767	0.9762	0.9930	0.9800	0.9898	0.9949	0.9997	0.9954
$U_{ref} = 20$ m s^{-1}	0.9887	0.9752	0.9728	0.9727	0.9702	0.9690	0.9897	0.9838	–

Conflict of Interest

The authors declare no conflicts of interest relevant to this study.

Data Availability Statement

Supplementary material including a picture of the investigated instrument, numerical schemes, wind tunnel validation results, tables of the numerical catch ratios and a sample set of flow velocity and drop trajectory maps are available in Chinchella et al. (2024b). URANS simulation results are described in Chinchella et al. (2021). The OpenFOAM software used to run simulations is open source and detailed in Jasak (2009).

References

Adirosi, E., Montopoli, M., Bracci, A., Porcù, F., Capozzi, V., Annella, C., et al. (2021). Validation of GPM rainfall and drop size distribution products through disdrometers in Italy. *Remote Sensing*, *13*(11), 2081. https://doi.org/10.3390/rs13112081

Adirosi, E., Porcù, F., Montopoli, M., Baldini, L., Bracci, A., Capozzi, V., et al. (2023). Database of the Italian disdrometer network. *Earth System Science Data*, *15*(6), 2417–2429. https://doi.org/10.5194/essd-15-2417-2023

Adirosi, E., Roberto, N., Montopoli, M., Gorgucci, E., & Baldini, L. (2018). Influence of disdrometer type on weather radar algorithms from measured DSD: Application to Italian climatology. *Atmosphere*, *9*(9), 360. https://doi.org/10.3390/atmos9090360

Alter, J. C. (1937). Shielded storage precipitation gages. *Monthly Weather Review*, *65*(7), 262–265. https://doi.org/10.1175/1520-0493(1937)65<262:SSPG>2.0.CO;2

Aqilah, F., Islam, M., Juretic, F., Guerrero, J., Wood, D., & Ani, F. N. (2018). Study of mesh quality improvement for CFD analysis of an airfoil. *IIUM Engineering Journal*, *19*(2), 203–212. https://doi.org/10.31436/iiumej.v19i2.905

Baire, Q., Dobre, M., Piette, A. S., Lanza, L., Cauteruccio, A., Chinchella, E., et al. (2022). Calibration uncertainty of non-catching precipitation gauges. *Sensors*, *22*(17), 6413. https://doi.org/10.3390/s22176413

Baker, T. J. (2005). Mesh generation: Art or science? *Progress in Aerospace Sciences*, *41*(1), 29–63. https://doi.org/10.1016/j.paerosci.2005.02.002

Bao, X., Wu, L., Zhang, S., Yuan, H., & Wang, H. (2020). A comparison of convective raindrop size distributions in the eyewall and spiral rainbands of Typhoon Lekima (2019). *Geophysical Research Letters*, *47*(23), e2020GL090729. https://doi.org/10.1029/2020GL090729

Beard, K. V. (1976). Terminal velocity and shape of cloud and precipitation drops aloft. *Journal of the Atmospheric Sciences*, *33*(5), 851–864. https://doi.org/10.1175/1520-0469(1976)033<0851:TVASOC>2.0.CO;2

Capozzi, V., Annella, C., Montopoli, M., Adirosi, E., Fusco, G., & Budillon, G. (2021). Influence of wind-induced effects on laser disdrometer measurements: Analysis and compensation strategies. *Remote Sensing*, *13*(15), 3028. https://doi.org/10.3390/rs13153028

Cauteruccio, A., Brambilla, E., Stagnaro, M., Lanza, L. G., & Rocchi, D. (2021). Wind tunnel validation of a particle tracking model to evaluate the wind-induced bias of precipitation measurements. *Water Resources Research*, *57*(7), e2020WR028766. https://doi.org/10.1029/2020WR028766

Cauteruccio, A., Chinchella, E., & Lanza, L. G. (2024). The overall collection efficiency of catching-type precipitation gauges in windy conditions. *Water Resources Research*, *60*(1), e2023WR035098. https://doi.org/10.1029/2023WR035098

Cauteruccio, A., Chinchella, E., Stagnaro, M., & Lanza, L. G. (2021). Snow particle collection efficiency and adjustment curves for the hotplate precipitation gauge. *Journal of Hydrometeorology*, *22*(4), 941–954. https://doi.org/10.1175/JHM-D-20-0149.1

Cauteruccio, A., & Lanza, L. G. (2020). Parameterization of the collection efficiency of a cylindrical catching-type rain gauge based on rainfall intensity. *Water*, *12*(12), 3431. https://doi.org/10.3390/w12123431

CEN. (2019). *EN 17277:2019; hydrometry—measurement requirements and classification of rainfall intensity measuring instruments*. European Committee for Standardization.

Chinchella, E., Cauteruccio, A., & Lanza, L. G. (2024a). The impact of wind on precipitation measurements from a compact piezoelectric sensor. *Journal of Hydrometeorology*, *25*(2), 339–352. In press. https://doi.org/10.1175/JHM-D-23-0180.1

Chinchella, E., Cauteruccio, A., & Lanza, L. G. (2024b). Supplementary to "Quantifying the wind-induced bias of rainfall measurements for the Thies optical disdrometer [Dataset]. *Zenodo*. https://doi.org/10.5281/zenodo.11633346

Chinchella, E., Cauteruccio, A., Stagnaro, M., & Lanza, L. G. (2021). Investigation of the wind-induced airflow pattern near the Thies LPM precipitation gauge. *Sensors*, *21*(14), 4880. https://doi.org/10.3390/s21144880

Colli, M., Pollock, M., Stagnaro, M., Lanza, L. G., Dutton, M., & O'Connell, E. (2018). A Computational Fluid-Dynamics assessment of the improved performance of aerodynamic rain gauges. *Water Resources Research*, *54*(2), 779–796. https://doi.org/10.1002/2017WR020549

de Moraes Frasson, R. P., Da Cunha, L. K., & Krajewski, W. F. (2011). Assessment of the Thies optical disdrometer performance. *Atmospheric Research*, *101*(1–2), 237–255. https://doi.org/10.1016/j.atmosres.2011.02.014

Derakhshandeh, J. F., & Alam, M. M. (2019). A review of bluff body wakes. *Ocean Engineering*, *182*, 475–488. https://doi.org/10.1016/j.oceaneng.2019.04.093

Ducros, F., Nicoud, F., & Poinsot, T. (1998). Wall-adapting local eddy-viscosity models for simulations in complex geometries. *Numerical Methods for Fluid Dynamics VI*, *6*, 293–299.

Folland, C. K. (1988). Numerical models of the raingauge exposure problem, field experiments and an improved collector design. *Quarterly Journal of the Royal Meteorological Society*, *114*(484), 1485–1516. https://doi.org/10.1002/qj.49711448407

Friedrich, K., Higgins, S., Masters, F. J., & Lopez, C. R. (2013). Articulating and stationary PARSIVEL disdrometer measurements in conditions with strong winds and heavy rainfall. *Journal of Atmospheric and Oceanic Technology*, *30*(9), 2063–2080. https://doi.org/10.1175/JTECH-D-12-00254.1

Ghiggi, G., Unal, C. M. H., Schleiss, M., Uijlenhoet, R., Raupach, T., & Berne, A. (2023). Disdrodb: A global data base of raindrop size distribution observations. In *40th conference on radar meteorology*. American Meteorological Society.

GmbH, Thies A., and Co, KG. (2011). *Instruction for use*. Adolf Thies GmbH and Co.

Green, M. J., & Helliwell, P. R. (1972). The effect of wind on the rainfall catch. In *Distribution of precipitation in mountainous areas. Proceedings of the Geilo Symposium, Norway, 31 July–5 August, 1972, WMO report 326*, (Vol. II, pp. 27–46). World Meteorological Organization.

Greenberg, S. (2001). *Ground based rainfall measurements at the NASA wallops flight facility* (Vol. 15). Pennsylvania State University.

Hunt, J. C., Wray, A. A., & Moin, P. (1988). Eddies, streams, and convergence zones in turbulent flows. Studying turbulence using numerical simulation databases. In *Proceedings of the 1988 summer program* (pp. 193–208). NASA Technical Reports, Stanford University Center for Turbulence Research.

Iserloh, T., Fister, W., Seeger, M., Willger, H., & Ries, J. B. (2012). A small portable rainfall simulator for reproducible experiments on soil erosion. *Soil and Tillage Research*, *124*, 131–137. https://doi.org/10.1016/j.still.2012.05.016

Jasak, H. (2009). OpenFOAM: Open source CFD in research and industry. *International Journal of Naval Architecture and Ocean Engineering*, *1*(2), 89–94. https://doi.org/10.2478/IJNAOE-2013-0011

Jevons, W. S. (1861). On the deficiency of rain in an elevated rain-gauge, as caused by wind. *Journal of the Franklin Institute*, *73*(5), 332. https://doi.org/10.1080/14786446108643180

Johannsen, L. L., Zambon, N., Strauss, P., Dostal, T., Neumann, M., Zumr, D., et al. (2020). Impact of disdrometer types on rainfall erosivity estimation. *Water*, *12*(4), 963. https://doi.org/10.3390/w12040963

Khvorostyanov, V. I., & Curry, J. A. (2005). Fall velocities of hydrometeors in the atmosphere: Refinements to a continuous analytical power law. *Journal of the Atmospheric Sciences*, *62*(12), 4343–4357. https://doi.org/10.1175/JAS3622.1

Kochendorfer, J., Earle, M., Rasmussen, R., Smith, C., Yang, D., Morin, S., et al. (2022). How well are we measuring snow post-SPICE? *Bulletin of the American Meteorological Society*, *103*(2), E370–E388. https://doi.org/10.1175/BAMS-D-20-0228.1

Lanza, L. G., & Cauteruccio, A. (2022). Accuracy assessment and intercomparison of precipitation measurement instruments. *Precipitation Science*, 3–35. Elsevier. https://doi.org/10.1016/B978-0-12-822973-6.00007-X

Lanza, L. G., Merlone, A., Cauteruccio, A., Chinchella, E., Stagnaro, M., Dobre, M., et al. (2021). Calibration of non-catching precipitation measurement instruments: A review. *Meteorological Applications*, *28*(3), e2002. https://doi.org/10.1002/met.2002

Lanza, L. G., & Vuerich, E. (2009). The WMO field intercomparison of rain intensity gauges. *Atmospheric Research*, *94*(4), 534–543. https://doi.org/10.1016/j.atmosres.2009.06.012

Marshall, J. S., & Palmer, W. Mc. K. (1948). The distribution of raindrops with size. *Journal of the Atmospheric Sciences*, *5*(4), 165–166. https://doi.org/10.1175/1520-0469(1948)005<0165:TDORWS>2.0.CO;2

Menter, F. R., Kuntz, M., & Langtry, R. (2003). Ten years of industrial experience with the SST turbulence model. In K. Hanjalic', Y. Nagano, & M. Tummers (Eds.), *Turbulence, heat and mass transfer 4* (Vol. 4, pp. 625–632). ©2003 Begell House, Inc.

Nešpor, V., Krajewski, W. F., & Kruger, A. (2000). Wind-induced error of raindrop size distribution measurement using a two-dimensional video disdrometer. *Journal of Atmospheric and Oceanic Technology*, *17*(11), 1483–1492. https://doi.org/10.1175/1520-0426(2000)017<1483:WIEORS>2.0.CO;2

Nešpor, V., & Sevruk, B. (1999). Estimation of wind-induced error of rainfall gauge measurements using a numerical simulation. *Journal of Atmospheric and Oceanic Technology*, *16*(4), 450–464. https://doi.org/10.1175/1520-0426(1999)016<0450:EOWIEO>2.0.CO;2

Pickering, B. S., Neely, R. R., & Harrison, D. (2019). The disdrometer verification network (DiVeN): A UK network of laser precipitation instruments. *Atmospheric Measurement Techniques*, *12*(11), 5845–5861. https://doi.org/10.5194/amt-12-5845-2019

Piomelli, U. (1999). Large-eddy simulation: Achievements and challenges. *Progress in Aerospace Sciences*, *35*(4), 335–362. https://doi.org/10.1016/S0376-0421(98)00014-1

Pope, S. B. (2001). *Turbulent flows*. Cambridge University Press.

Robinson, A. C., & Rodda, J. C. (1969). Rain wind and aerodynamic characteristics of rain-gauges. *The Meteorological Magazine*, *98*(1161), 113.

Testik, F. Y., & Pei, B. (2017). Wind effects on the shape of raindrop size distribution. *Journal of Hydrometeorology*, *18*(5), 1285–1303. https://doi.org/10.1175/JHM-D-16-0211.1

Thériault, J. M., Rasmussen, R., Ikeda, K., & Landolt, S. (2012). Dependence of snow gauge collection efficiency on snowflake characteristics. *Journal of Applied Meteorology and Climatology*, *51*(4), 745–762. https://doi.org/10.1175/JAMC-D-11-0116.1

Thériault, J. M., Rasmussen, R., Petro, E., Trépanier, J. Y., Colli, M., & Lanza, L. G. (2015). Impact of wind direction, wind speed, and particle characteristics on the collection efficiency of the double fence intercomparison reference. *Journal of Applied Meteorology and Climatology*, *54*(9), 1918–1930. https://doi.org/10.1175/JAMC-D-15-0034.1

Uijlenhoet, R., & Torres, D. S. (2006). Measurement and parameterization of rainfall microstructure. *Journal of Hydrology*, *328*(1–2), 1–7. https://doi.org/10.1016/j.jhydrol.2005.11.038

Upton, G., & Brawn, D. (2008). An investigation of factors affecting the accuracy of Thies disdrometers. In *WMO technical conference on instruments and methods of observation (TECO-2008)* (pp. 27–29). Russian Federation.

WMO. (2018). *Guide to instruments and methods of observation*. World Meteorological Organization. ISBN 978-92-63-10008-5.

Wolff, M. A., Isaksen, K., Petersen-Øverleir, A., Ødemark, K., Reitan, T., & Brækkan, R. (2015). Derivation of a new continuous adjustment function for correcting wind-induced loss of solid precipitation: Results of a Norwegian field study. *Hydrology and Earth System Sciences*, *19*(2), 951–967. https://doi.org/10.5194/hess-19-951-2015